

Diese Arbeit wurde vorgelegt am Aerodynamischen Institut

# Investigations on two-way coupling effects of particle-laden decaying isotropic turbulent flows

---

PROJEKTARBEIT  
VON  
JULIAN STEMMERMAN, STEFFEN TRIENEKENS  
UND CHRISTIAN SOIKA

---

Aerodynamisches Institut der RWTH Aachen

November 21, 2017

Betreuer: Konstantin Fröhlich

Erstprüfer: Univ.-Prof. Dr.-Ing. Wolfgang Schröder

# Contents

<b>I</b>	<b>Nomenclature</b>	<b>I</b>
<b>1</b>	<b>Introduction</b>	<b>1</b>
<b>2</b>	<b>Mathematical models</b>	<b>3</b>
2.1	Equations governing the fluid phase . . . . .	3
2.2	Scales of turbulent flows . . . . .	4
2.3	Particle dynamics . . . . .	5
<b>3</b>	<b>Numerical methods</b>	<b>7</b>
3.1	Discretization of the particle dynamics . . . . .	7
3.2	Direct numerical simulation . . . . .	7
3.3	Large-eddy simulation . . . . .	8
3.4	Computational point particles . . . . .	9
3.5	Applied simulation . . . . .	9
<b>4</b>	<b>Results</b>	<b>10</b>
4.1	Turbulence modulation by particles . . . . .	10
4.2	Simulation setup . . . . .	11
4.3	Simulation results . . . . .	12
<b>5</b>	<b>Conclusion and outlook</b>	<b>15</b>
<b>6</b>	<b>References</b>	<b>16</b>
<b>7</b>	<b>Appendix A</b>	<b>18</b>

# I Nomenclature

## Acronyms

DNS	Direct numerical simulation
ILES	Implicit large-eddy simulation
LES	Large-eddy simulation
PP	Particle-laden simulation
SGS	Subgrid scale
sP	Single-phase simulation

## Greek Symbols

$\Delta$	Cell length
$\varepsilon$	Integral dissipation rate
$\varepsilon'$	Additional integral particle induced dissipation rate
$\bar{\varepsilon}$	Integral dissipation rate of the flow field
$\gamma$	Isentropic exponent
$\eta$	Kolmogorov length scale
$\mu$	Dynamic viscosity
$\lambda_c$	Ratio of physical point particles to computational point particles
$\nu$	Kinematic viscosity
$\phi_m$	Mass fraction
$\phi_v$	Volume fraction
$\Psi$	Integral coupling rate
$\Psi_p$	Coupling rate for one particle
$\Psi_{pp}$	Integral coupling rate using the point-particle approach
$\rho$	Fluid density
$\rho_p$	Particle density
$\sigma$	Smoothing parameter
$\bar{\tau}$	Stress tensor
$\tau_\eta$	Kolmogorov time scale
$\tau_L$	Eddy turnover time
$\tau_p$	Particle response time
$\omega_p$	Particle angular velocity vector
$\Upsilon_f$	Full fluid domain

## Operators

$\frac{D}{Dt}$	Time derivative following a fluid unit
$\frac{d}{dt}$	Time derivative
$\delta$	Small step of the following variable
$\frac{\partial}{\partial t}$	Partial derivative with respect to time

$\nabla$	Nabla operator
$:$	Inner tensor product
<b>Roman Symbols</b>	
$A$	Control surface
$\mathbf{a}_p$	Particle acceleration
$C_d$	Empirical drag coefficient
$c_p$	Specific isobaric heat capacity
$c_v$	Specific isochoric heat capacity
$d_i$	Distance between particle position and center of the cell
$d_p$	Particle diameter
$E$	Specific inner energy
$e$	Specific internal energy
$E_k$	Turbulent kinetic energy of the fluid
$E_{kB}$	Turbulent kinetic energy of the particles
$\mathbf{F}$	Force vector per unit volume of the particle acting on the fluid
$f_D$	Drag correction
$\mathbf{F}_{pp}$	Sum vector of forces acting on the particles
$\mathbf{F}_p$	Particle surface force vector
$G(r)$	Filter function
$\bar{\mathbf{H}}$	Flux tensor
$\bar{\mathbf{H}}^i$	Inviscid part of the flux tensor
$\bar{\mathbf{H}}^v$	Viscous part of the flux tensor
$\bar{\mathbf{I}}$	Identity tensor
$k_t$	Thermal conductivity
$L$	Integral length scale
$Ma$	Mach number
$m_p$	Particle mass
$\mathbf{n}$	Normal vector
$N$	Grid refinement of the simulation
$N_c$	Number of computational point particles
$N_p$	Number of physical point particles
$p$	Pressure
$Pr$	Prandtl number
$\mathbf{Q}$	Vector of conservative Eulerian variables
$\mathbf{q}$	Heat conduction vector
$R$	Specific gas constant
$Re$	Reynolds number
$Re_p$	Particle Reynolds number

$\bar{\mathbf{S}}$	Rate-of-strain tensor
$S$	Sutherland temperature
$T$	Temperature
$t$	time
$t^*$	Time normalized by initial eddy turnover time
$\mathbf{T}_p$	Particle torque vector
$\mathbf{u}$	Fluid velocity
$U$	Characteristic fluid velocity
$\mathbf{u}'$	Vector of fluid velocity fluctuations
$\mathbf{u}_p$	Vector of fluid velocity at the particle position
$V$	Control volume
$V_p$	Particle volume
$\mathbf{v}_p$	Particle velocity vector
$v_r$	Relative velocity between particle and fluid
$\mathbf{x}$	Position vector
$\mathbf{x}_p$	Particle position vector

# 1 Introduction



Figure 1: Photograph courtesy of Hassan Nagib and Thomas Corke. Formation of a nearly isotropic turbulent flow field behind a grid [7].

Particle-laden turbulent flows are ubiquitous in nature. Spray atomization in fuel injectors, cyclonic particle separation in oil refineries and sediment accumulation in pipelines are examples for technical applications, where it is of huge interest to predict the impact of the particles on turbulent flows. Turbulence augmentation or attenuation by particles is therefore a decisive factor.

A study about the impact of particles on the isotropic decaying turbulent flow is presented. Incompressible, isothermal and isotropic decaying turbulence will serve as the carrier flow. Gravity is omitted to avoid prominent directions. Isotropic turbulence is a relatively good assumption when a small region of a high-Reynolds-number flow, which is not affected by boundary effects, is observed [3]. This fact is visualized by Fig 1. Describing turbulent flows is a large task because of the involvement of many different scales of turbulent motion.

In this work the influence of the particles on the isotropic decaying turbulence is numerically calculated by using direct numerical (DNS) and large-eddy simulations (LES). Direct numerical simulations are able to resolve all scales of turbulent motion due to their high grid refinement. Large-eddy simulations have a lower grid resolution and use therefore a subgrid-scale model (SGS) to model these scales. This type of simulation therefore has a lower computational effort.

The simulations were carried out using the point-particle approach, where each

particle is tracked via a Lagrangian approach. The feedback of the particles on the flow field is modeled by sources and sinks, which is referred to as two-way coupling. Alternatives are one-way coupling, at which only the flow exerts influence on the particles, and four-way coupling, which extends two-way coupling by particle-particle interactions. Two-way coupling is fitting for the simulations in this study, because the volume fraction  $\phi_v = 10^{-3}$  of the particles is large enough to alter the turbulence. Volume fractions below  $\phi_v = 10^{-6}$  are referred to as one-way coupling and the interactions that can be observed at values greater than  $\phi_v = 10^{-3}$  are called four-way coupling [14] [15]. The particle diameter is defined to be smaller than the Kolmogorov scale, i.e. the smallest scale of the turbulent flow. The particle density is much higher than the fluid density.

To lower the computational effort in general, a new variable, which describes the fraction of physical to numerical point particles, is introduced and validated.

The structure of this work is described in the following. First, mathematical models for single-phase and particle dynamics are given. Additionally, the scales of turbulent motion are described. Thereafter, the computational basics of both DNS and LES and their respective advantages and disadvantages are explained. Subsequently, the used discretization method to integrate the particle tracking equations is described and the 'computational point particles', in the following referred to as CPP, are introduced. The CPP approach is validated by analyzing turbulent kinetic energy budgets for LES and DNS. Also the number of particles that is needed to get consistent average values for the flow characteristics is investigated. Finally, a short conclusion is given.

## 2 Mathematical models

In this section the Navier-Stokes equations in integral formulation, the characteristic turbulent scales and the kinematic and dynamic equations for the particle phase are introduced.

### 2.1 Equations governing the fluid phase

The conservation of mass, momentum and energy for a control volume  $V$  reads

$$\int_V \frac{\partial \mathbf{Q}}{\partial t} dV + \int_{\partial V} \bar{\mathbf{H}} \cdot \mathbf{n} dA = \mathbf{0} \quad (2.1)$$

with time  $t$  and the flux tensor  $\bar{\mathbf{H}}$ . The vector  $\mathbf{Q}$  contains the variables fluid density  $\rho$ , fluid velocity  $\mathbf{u}$  and specific inner energy  $E$ :

$$\mathbf{Q} = \begin{pmatrix} \rho \\ \rho \mathbf{u} \\ \rho E \end{pmatrix}. \quad (2.2)$$

$\bar{\mathbf{H}}$  is the flux tensor which contains the inviscid and viscous flux, i.e.

$$\bar{\mathbf{H}} = \bar{\mathbf{H}}^i + \bar{\mathbf{H}}^v = \begin{pmatrix} \rho \mathbf{u} \\ \rho \mathbf{u} \mathbf{u} + p \\ \mathbf{u}(\rho E + p) \end{pmatrix} - \frac{1}{Re} \begin{pmatrix} 0 \\ \bar{\boldsymbol{\tau}} \\ \bar{\boldsymbol{\tau}} \mathbf{u} + \mathbf{q} \end{pmatrix}, \quad (2.3)$$

with the shear stress  $\bar{\boldsymbol{\tau}}$ , heat conduction  $\mathbf{q}$  and the pressure  $p$ . The Reynolds number  $Re = \frac{\rho_\infty u_\infty l_{\text{ref}}}{\mu_\infty}$  is defined to be the ratio of inertia forces to viscous forces with reference density  $\rho_\infty$ , velocity  $u_\infty$ , length  $l_{\text{ref}}$  and dynamic viscosity  $\mu_\infty$ .

The specific inner energy  $E$  and the heat conduction  $\mathbf{q}$  are defined as

$$E = e \frac{1}{2} |\mathbf{u}|^2 \text{ and} \quad (2.4)$$

$$\mathbf{q} = -\frac{\mu}{Pr(\gamma - 1)} \nabla T, \quad (2.5)$$

with the constant capacity ratio  $\gamma = \frac{c_p}{c_v}$  and the Prandtl number  $Pr = \frac{\mu_\infty c_p}{k_t}$  using the specific heat capacities of the fluid  $c_v$  and  $c_p$  and thermal conductivity  $k_t$ . Assuming that the fluid is newtonian, the Stokes hypothesis yields

$$\bar{\boldsymbol{\tau}} = 2\mu \bar{\mathbf{S}} - \frac{2}{3}\mu(\nabla \cdot \mathbf{u})\bar{\mathbf{I}}, \quad (2.6)$$

in which  $\bar{\mathbf{S}} = \frac{(\nabla \mathbf{u})(\nabla \mathbf{u})^T}{2}$  denotes the rate-of-strain tensor. Additionally, the viscosity  $\mu$  can be approximated by Sutherland's law

$$\mu(T) = \mu_\infty \left( \frac{T}{T_\infty} \right)^{3/2} \frac{T_\infty + S}{T + S}, \quad (2.7)$$



where  $S$  is the Sutherland temperature. To achieve closure the caloric state equation  $e = c_v T$  and the state equation for an ideal gas  $p = \rho R T$  are used. The specific gas constant is determined by  $R = c_p - c_v$ .

## 2.2 Scales of turbulent flows

Turbulent flows can be described as a superposition of chaotic, three-dimensional vortical structures of various scales (eddies). Larger eddies decay and pass their kinetic energy down to smaller scales. At the smallest scales, the kinetic energy finally dissipates into heat due to the viscous dissipation. This behavior is called the 'energy cascade' and was first described by Richardson [11] and quantified by Kolmogorov [3].

The first set of scales describe the large eddies. At these scales the energy is brought into the flow, creating the 'energy-containing range'. The corresponding timescale, which is most times called 'eddy turnover time', is defined as

$$\tau_L = \frac{L}{U}, \quad (2.8)$$

with the integral length scale  $L$  (2.16) and the characteristic fluid velocity  $U$ .

The smallest scales in a turbulent flow are the Kolmogorov length  $\eta$  and time scale  $\tau_\eta$ . At these scales, the effects of viscosity take place and the energy dissipates into heat. With the estimate  $\epsilon \approx \frac{U^3}{L}$  they can be written as

$$\eta = \left( \frac{\nu^3 L}{U^3} \right)^{1/4} \quad (2.9)$$

and

$$\tau_\eta = \left( \frac{\nu L}{U^3} \right). \quad (2.10)$$

Both these scales are coupled by the Reynolds numbers

$$\frac{L}{\eta} = Re^{3/4} \quad (2.11)$$

and

$$\frac{\tau_L}{\tau_\eta} = Re_L^{1/2}. \quad (2.12)$$

It can be observed from these equations that the spacing between the scales increases for higher Reynolds numbers.

Characteristic length scales  $\lambda$  and  $L$  of a turbulent flow can be defined by the two-point correlation  $R$ , which is the normalized product of the velocity's fluctuation  $\mathbf{u}'$  at two different positions  $\mathbf{x}$  and  $\mathbf{x} + \mathbf{r}$  at the same time  $t$

$$R(\mathbf{x}, \mathbf{r}) = \frac{\overline{\mathbf{u}'(\mathbf{x}, t) \mathbf{u}'(\mathbf{x} + \mathbf{r}, t)}}{\sqrt{\overline{\mathbf{u}'^2(\mathbf{x}, t)}} \sqrt{\overline{\mathbf{u}'^2(\mathbf{x} + \mathbf{r}, t)}}}, \quad (2.13)$$

as

$$\frac{1}{\lambda^2} = -\frac{1}{2} \left( \frac{\partial^2 R}{\partial \mathbf{r}^2} \right), \quad (2.14)$$

$$\lambda = \sqrt{15 \frac{\nu}{\epsilon}} |\mathbf{u}'| \quad (2.15)$$

or

$$L = \int_0^\infty R(\mathbf{x}, \mathbf{r}) d\mathbf{r} \quad (2.16)$$

with  $\lambda$  being the Taylor microscale,  $L$  the integral length scale and  $|\mathbf{u}'|$  denoting the absolute value of the velocity's fluctuation.

The Taylor microscale can be used to compute the Taylor-scale Reynolds number

$$Re_\lambda = \frac{|\mathbf{u}'| \lambda}{\nu}. \quad (2.17)$$

### 2.3 Particle dynamics

To take the forces acting from the particles on the fluid into account the Navier-Stokes equation for the carrier fluid (2.3) is extended by the force  $\mathbf{F}$  that acts on the ambient cells with different intensity regarding on the distance between these cells and the particle

$$\mathbf{F} = \mathbf{F}_{pp} \cdot \frac{e^{-(d_i^2/(\sigma\Delta^2))}}{\sum_i e^{-(d_i^2/(\sigma\Delta^2))}}, \quad (2.18)$$

with the distance between particle position and midpoint of the cell  $d_i$ , the length of the cells  $\Delta$  and a smoothing parameter  $\sigma$  that controls the distribution of  $\mathbf{F}$  on the adjacent cells.  $\mathbf{F}_{pp}$  is the sum of pressure and shear forces acting on the particles and is described explicitly in the Maxey-Riley equation that can be achieved from [12].  $\mathbf{F}_{pp}$  can be divided into several forces. Reduced to the governing forces acting on the particles and with neglect of gravity the dynamic equation of the particles becomes

$$\begin{aligned} \mathbf{F}_{pp} = m_p \frac{d\mathbf{v}_p}{dt} = \rho V_p \frac{D\mathbf{u}}{Dt} - \frac{3}{4} \rho V_p \frac{C_d}{d_p} |\mathbf{v}_p - \mathbf{u}| (\mathbf{v}_p - \mathbf{u}) + \frac{1}{2} \rho V_p \left( \frac{D\mathbf{u}}{Dt} - \frac{d\mathbf{v}_p}{dt} \right) + \\ \frac{3}{2} d_p^2 \rho \sqrt{\pi \nu} \int_{t_0}^t \frac{dt'}{(t - t')^{1/2}} \left( \frac{D\mathbf{u}}{Dt} - \frac{d\mathbf{v}_p}{dt} \right). \end{aligned} \quad (2.19)$$

$\mathbf{v}_p(\mathbf{x}_p, t)$  is the particle velocity vector with the time derivative  $d/dt$  following a sphere while  $D/Dt$  is the time derivative following a fluid unit. The individual forces on the right side of the equation are stated in the following:

- $\rho V_p \frac{D\mathbf{u}}{Dt}$ :  
pressure gradient of the undisturbed flow
- $-\frac{3}{4}\rho V_p \frac{C_d}{d_p} |\mathbf{v}_p - \mathbf{u}|(\mathbf{v}_p - \mathbf{u})$ :  
hydrodynamical drag force that is parallel to the undisturbed streamlines, which depends on an empirical drag coefficient  $C_d$  defined by Schiller and Naumann as  $C_d = \frac{24}{Re_p}(1 + 0.15Re_p^{0.687})$ . It is described by the Stokes' law as the force of viscosity acting on the interface of small spherical particles and fluid that can be achieved at very low Reynolds numbers in a viscous fluid
- $\frac{1}{2}\rho V_p \left( \frac{D\mathbf{u}}{Dt} - \frac{d\mathbf{v}_p}{dt} \right)$ :  
added mass force, representing the influence of the fluid's inertia that has an impact on the particle, in case of a different acceleration than the particles
- $\frac{3}{2}d_p^2\rho\sqrt{\pi\nu} \int_{t_0}^t \frac{dt'}{(t-t')^{1/2}} \left( \frac{D\mathbf{u}}{Dt'} - \frac{d\mathbf{v}_p}{dt'} \right)$ :  
history force taking diffusion and convection into account that results from vortices in the slipstream of the particles

As presented by Vincenzo Armenio and Virgilio Fiorotto [17] compared to the Stokes drag all other forces could be neglected with rising particle density, so due to the density ratio being  $\rho_p/\rho \gg 1$ ,  $\mathbf{F}_{pp}$  can be approximately reduced to the dominating viscous drag. (2.19) becomes

$$\mathbf{F}_{pp} = m_p \frac{d\mathbf{v}_p}{dt} = \frac{3}{4}\rho V_p \frac{C_d}{d_p} |\mathbf{v}_p - \mathbf{u}|(\mathbf{v}_p - \mathbf{u}). \quad (2.20)$$

Using the particle Reynolds number  $Re_p = \frac{v_r d_p}{\nu}$  with the relative velocity between particle and fluid  $v_r$ , (2.20) can be compressed, which is described in detail in [2].

$$\rho_p \frac{d\mathbf{v}_p}{dt} = \rho_p \frac{\mathbf{v}_p - \mathbf{u}}{\tau_p} f_d. \quad (2.21)$$

Here the particle response time  $\tau_p = \frac{(\rho_p/\rho)d_p^2}{18\nu}$  is introduced which is a time constant in the exponential decay of the particle velocity as a result of an upcoming fluid drag and physically represents the time scale over which the drag force decreases the particle's relative velocity to zero.  $f_d = 1 + 0.15Re_p^{0.687}$  is a correction factor depending on the flow conditions. Together with the kinematic equation of a particle

$$\frac{d\mathbf{x}_p}{dt} = \mathbf{v}_p, \quad (2.22)$$

the adjusted equation (2.3) and (2.21) form the basic equations for the particle laden system.

### 3 Numerical methods

Two numerical methods are discussed and their main differences pointed out in the following chapter, the DNS (direct numerical simulation) and the LES (large-eddy simulation). The basis of both are the Navier-Stokes equations as described above.

#### 3.1 Discretization of the particle dynamics

To integrate the Lagrangian particle tracking equations, discussed before, a predictor-corrector scheme based on the trapezoidal rule for numerical integration

$$f(t + \delta t) \approx f(t) + \frac{\delta t}{2} \left[ \frac{\partial f(t)}{\partial t} + \frac{\partial f(t + \delta t)}{\partial t} \right] \quad (3.1)$$

is used.

The first step is the prediction of the new particle position  $\mathbf{x}_{p,n+1}$  using a Taylor expansion for a small time step  $\delta t$

$$\mathbf{x}_{p,n+1} = \mathbf{x}_{p,n} + \delta t \mathbf{v}_{p,n} + \frac{1}{2} \delta t^2 \mathbf{a}_{p,n}, \quad (3.2)$$

with  $\mathbf{a}_{p,n}$  particle acceleration.

To avoid filtering effects, the fluid velocity  $\mathbf{u}(\mathbf{x}_{p,n+1})$  at the particle position  $\mathbf{x}_{p,n+1}$  is set equal to the nearest cell fluid velocity.

The updated velocity and acceleration are calculated as

$$\mathbf{v}_{p,n+1} = \frac{\mathbf{v}_{p,n} + \frac{1}{2} \delta t \left( \mathbf{a}_{p,n} + \frac{f_d}{\tau_p} \mathbf{u}(\mathbf{x}_{p,n+1}) \right)}{1 + \frac{1}{2} \frac{f_D}{\tau_p} \delta t}, \quad (3.3)$$

$$\mathbf{a}_{p,n+1} = \frac{\frac{f_D}{\tau_p} (\mathbf{u}(\mathbf{x}_{p,n+1}) - \mathbf{v}_{p,n}) - \frac{1}{2} \delta t \mathbf{a}_{p,n}}{1 + \frac{1}{2} \frac{f_D}{\tau_p} \delta t}. \quad (3.4)$$

The updated particle position must be corrected by an additional term according to the trapezoidal rule

$$\mathbf{x}_{p,n+1} = \mathbf{x}_{p,n} + \frac{1}{2} \delta t (\mathbf{v}_{p,n+1} + \mathbf{v}_{p,n}) + \frac{1}{12} \delta t^2 (\mathbf{a}_{p,n+1} - \mathbf{a}_{p,n}). \quad (3.5)$$

#### 3.2 Direct numerical simulation

With DNS, the Navier-Stokes equations are solved completely. This provides a very accurate result, as all scales of motion are being resolved. Still it requires

an immense level of computational resources which increases rapidly with the Reynolds number:  $N^3 \propto 4.4Re_L^{9/4} \approx 0.06Re_\lambda^{9/2}$  with gridsize  $N$  of the simulation. These computational resources were not available until the 1970s. With the LES, as described below, the computational effort is 99.98 % less compared to DNS, which indeed is the fraction of the dissipative scale. This leaves 0.02 % of the flow, which is correlative with the fraction of the energy-containing larger-scale [13].

### 3.3 Large-eddy simulation

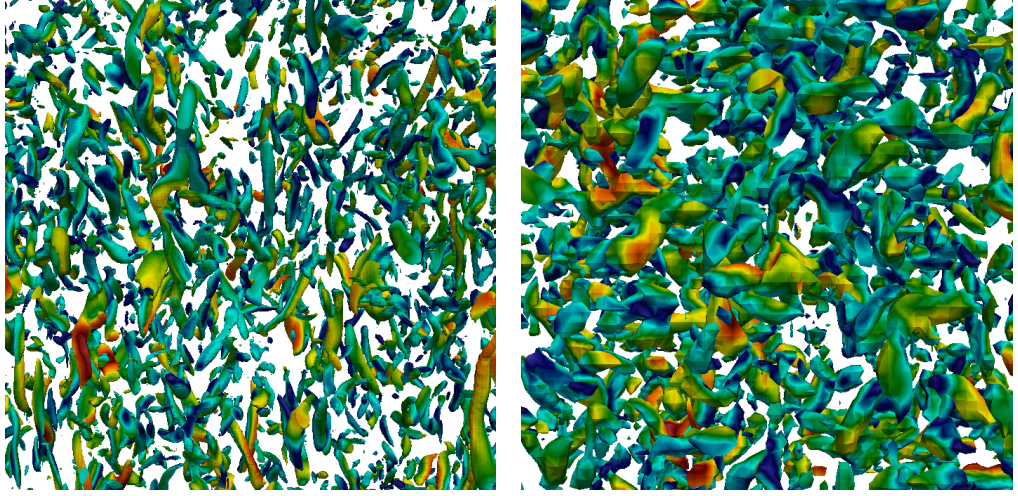


Figure 2: Comparison between DNS and LES. 'Worm-like' structures in an isotropic flow field simulated in different grid resolutions. The more refined grid on the left show more and better resolved structures, while the right picture reveals more artificially generated artifacts. For creation see Appendix A.

Due to the fact that DNS is effortful, LES was created to save time and resources. The energy containing larger-scale motion is completely resolved and the small effects of the smaller-scale motion are modeled. Otherwise in DNS resolving the small dissipative scale would require most of the computational resources.

Simulating only the larger-scale motions is called filtering, which means that the smaller-scale motions, also known as fluctuation, are filtered out. The filtered velocity field is calculated by  $\bar{U}(\mathbf{x}) = \int_{-\infty}^{\infty} G(\mathbf{r})U(\mathbf{x} - \mathbf{r})d\mathbf{r}$ , with  $G(\mathbf{r})$  being a homogeneous filter function. For further information on filter functions, the works of Pope [13] should be considered. To model the filtered smaller-scale motions usually a subgrid-scale (SGS) model is used. According to Hickel (2007) the interference between explicit SGS and the truncation error can be exploited, i.e. the truncation error can serve as model of the effects of unresolved scales, which is therefore an implicit SGS model. Thus it is called implicit LES (ILES) [16].

### 3.4 Computational point particles

The high number of point particles requires even more computational resources for the particle-laden simulations than for the single-phase simulations. The idea to reduce this requirement is to create clusters of point particles. For this purpose the ratio  $\lambda_c$  of physical point particles  $N_p$  to CPPs  $N_c$  is introduced ( $\lambda_c = \frac{N_p}{N_c}$ ). To compensate this lack of particles, the coupling force is multiplied by  $\lambda_c$ , due to the  $\lambda_c$ -fold mass of the (cluster-)particles.

### 3.5 Applied simulation

The simulations were carried out using ZFS, the simulation tool developed and implemented at the Institute of Aerodynamics at RWTH Aachen University [5] [6]. The tool is capable of simulating finite-volume flows of compressible fluids. In the simulations, which results the reader can see at hand, the Mach-number  $Ma$  was set to 0.1 to simulate an almost incompressible fluid.

## 4 Results

In this section, the properties and results of the DNS and LES of particle-laden decaying isotropic turbulence which have been carried out will be presented. An additional test to find out which CPP-factor could be used is presented. Special emphasis will be put on the turbulent kinetic energy budgets and their use to interpret the findings.

### 4.1 Turbulence modulation by particles

The particle-laden decaying isotropic turbulence is determined by the coupling rate  $\Psi$ , which describes the energy transfer between both fluid and particle phase, the background (Begriff pruefen!!!) dissipation rate  $\bar{\epsilon}$  and the particle-induced dissipation rate  $\epsilon'$ :

$$\frac{dE_k}{dt} = \Psi(t) - \bar{\epsilon}(t) - \epsilon'(t). \quad (4.1)$$

In this equation,  $\bar{\epsilon}(t)$  displays the dissipation rate of the flow field and  $\epsilon'(t)$  is the additional dissipation rate introduced by the injected point-particles. As the dissipation rate is always of positive value, it acts as a sink for the fluid's turbulent kinetic energy. In difference to that, the coupling rate can serve either as source or sink, depending on the acceleration of the particles [1]. The coupling rate for fully resolved particles  $\Psi$  is defined as

$$\Psi(t) = \sum_{p=1}^{N_p} \Psi_p = - \sum_{p=1}^{N_p} (\mathbf{F}_p \cdot \mathbf{v}_p + \mathbf{T}_p \cdot \boldsymbol{\omega}_p), \quad (4.2)$$

using surface force  $\mathbf{F}_p$ , particle velocity  $\mathbf{v}_p$ , torque  $\mathbf{T}_p$  and angular velocity  $\boldsymbol{\omega}_p$  to describe the transfer of kinetic energy resulting at each particle. The torque can be neglected for the used point-particle approach.

As mentioned before, the flow field is considered nearly incompressible, therefore the equation for the viscous dissipation rate can be approximated by

$$\epsilon(t) \approx 2\mu \bar{\mathbf{S}} : \bar{\mathbf{S}}, \quad (4.3)$$

where  $:$  denotes the inner tensor product. This rate can then be integrated over the fluid domain excluding particles and their direct surroundings  $\Upsilon_f$ , leading to

$$\bar{\epsilon}(t) = \int_{\Upsilon_f} \epsilon(t) dV. \quad (4.4)$$

Additionally the particles change the fluid's rate of dissipation  $\epsilon$  due to their volume forces. The additional dissipation rate for fully resolved particles can be

computed by

$$\varepsilon' = \sum_{p=1}^{N_p} \mathbf{F}_p \cdot (\mathbf{u}_p - \mathbf{v}_p), (Gleichungergaenzen) \quad (4.5)$$

using the velocity of the fluid  $\mathbf{u}_p$  at the particle position.

$$\frac{dE_k}{dt} = \mathbf{F} \cdot \mathbf{u} - \bar{\varepsilon} \quad (4.6)$$

For  $\rho_p \gg \rho$  and the point-particle approach the coupling rate  $\Psi$  and the additional dissipation rate  $\varepsilon'$  are implicitly coupled:

$$\Psi_{pp}(t) = \Psi - \varepsilon'(t) = - \sum_{p=1}^{N_p} \mathbf{F}_p \cdot \mathbf{u}_p. \quad (4.7)$$

This leads to

$$\frac{dE_k}{dt} = \Psi_{pp}(t) - \varepsilon(t). \quad (4.8)$$

## 4.2 Simulation setup

All cases were simulated on a cubic domain and a Cartesian grid using different grid refinement levels. For the LES-cases  $64^3$ ,  $96^3$  and  $128^3$  are employed, hence the need to model smaller scales with SGS-models, which have already been validated in [9]. For a DNS,  $256^3$  cells are necessary to resolve all scales.

The particle-free case was initialized using a seed-based number random generator, which is described in detail in [?]. At the initial eddy turnover time  $t^* = t \frac{\varepsilon_0}{u_0^2} \approx 0.27$ , using the initial viscous dissipation rate  $\varepsilon_0$  and initial rms-velocity  $u_0$ , a restart file is written out to initialize the subsequent simulation of the particle-laden isotropic turbulence. This file is then used to set up a second simulation, where the particles are initialized at random positions with the fluid velocity. The single-phase DNS and particle-laden DNS will be used as reference for analyzing other results. The single-phase results will be in the following referred to as sP, and particle-laden results as PP. The PP simulations are set up to match the volume fraction  $\phi_v = \frac{V_p}{V_f} = 10^{-3}$  and mass fraction of  $\phi_m = \frac{m_p}{m_f} = 1$ . The density ratio was set to  $\frac{\rho_p}{\rho} = 1000$  and the particle diameter is  $d_p \approx 0.6\eta_0$  with  $\eta_0$  being the initial Kolmogorov length. At the timestep of injection the particle response time  $\tau_p$  was ??? and  $Re_\lambda \approx 58$ .



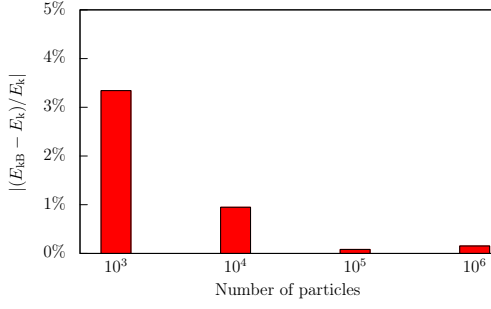


Figure 3: Initializing different numbers of point-particles on a  $128^3$ -grid. An inaccuracy can be observed for small numbers of particles. This behavior can be observed for all other resolutions.

### 4.3 Simulation results

The first set of simulation was set up to investigate how different numbers of injected particles have an influence on the difference of turbulent kinetic energy of both particle and fluid. As mathematical description of turbulent flows is based on statistics, small numbers of particles can lead to questionable results. An example for the deviation in kinetic energy for different numbers of particles can be found in Fig. 3. The normalized difference in kinetic energy  $E_{kB}$  of the particles and the flow itself  $E_k$  shows a correlation between particle number and accuracy in in this single simulation. Although this was just a single initialization of particles in a flow, it can be stated that simulations using only  $10^3$  or even up to  $10^4$  particles are not accurate enough for technical or scientific use of data. Simulations in other grid sizes show similar results.

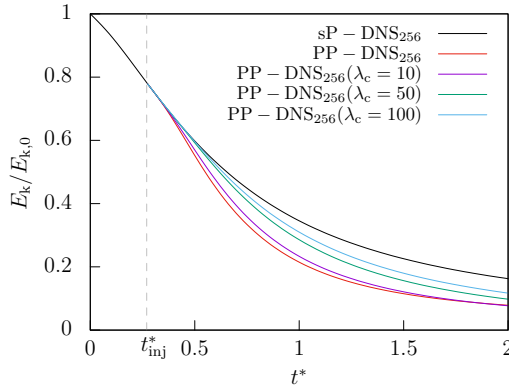


Figure 4: Kinetic energy  $E_k$  normalized by its initial value  $E_{k,0}$  over time normalized by initial eddy turnover time. Shortly after the injection the PP-cases separates from the sP-flow. The higher-clustered cases show less distinctions from the sP-case.

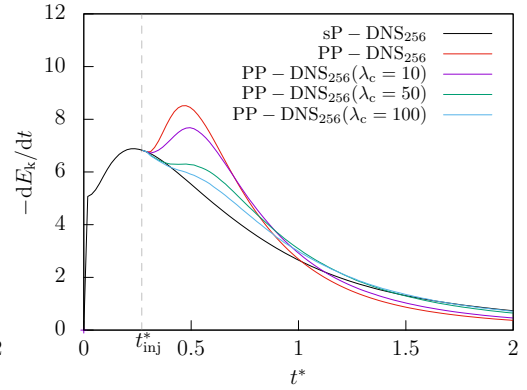


Figure 5: Change in kinetic energy over time normalized by initial eddy turnover time. After  $t^* \approx 1$  the unclustered PP-case shows a lower decay rate in kinetic energy than the sP-case.

The second set of simulations conducted in this work is set up to investigate the influence of CPPs on the accuracy of the simulations with the goal to minimize

computational effort, while still achieving high quality results. For this purpose, the variable  $\lambda_c$ , which was established before, was implemented in the program code. The simulations were then set up with the overall same number of a million particles, altering just  $\lambda_c$ . It can be seen in Fig. 4 and 5 that the decay in kinetic energy from the injection point depends highly on the number of clustered particles. It can be stated that the flow's statistics for high  $\lambda_c$  converge towards the sP-case.

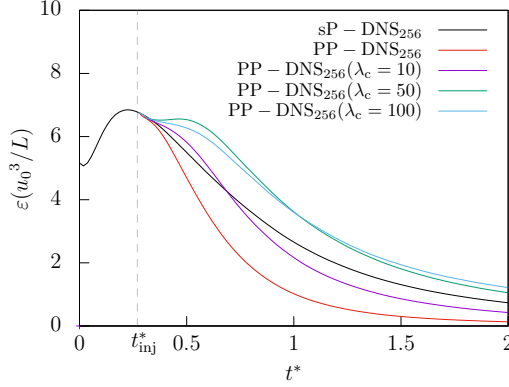


Figure 6: Normalized dissipation rate  $\bar{\epsilon}$  over time normalized by initial eddy turnover time. The unclustered PP-case shows a lower dissipation rate than the sP-case. Highly clustered PP-cases show a higher dissipation rate.

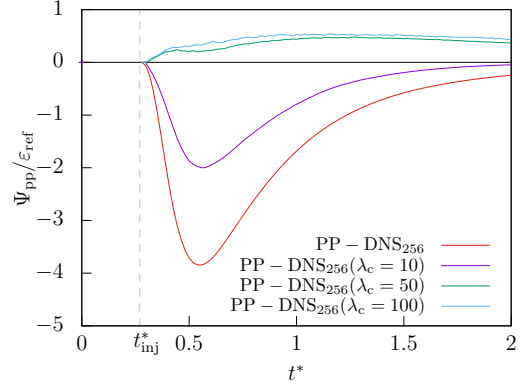


Figure 7: Normalized point-particle coupling rate  $\Psi_{pp}$  over time normalized by initial eddy turnover time. The PP-case without clustering shows the lowest coupling rate. Both highly-clustered PP-cases show physically questionable behavior.

Fig. 6 and 7 can be interpreted using the turbulent kinetic energy budget introduced earlier. The PP-case without clustering shows a lower dissipation rate than the sP-case, both highly-clustered cases show a higher rate over the monitored period of time, which is an unphysical behavior. The coupling rate is negative the whole time for the PP-cases with lower  $\lambda_c$  and positive for the higher-clustered cases. Both these effects form the change in kinetic energy in particle-laden isotropic flow found in Fig. 5.

Being very similar in the time shortly after the injection, the flow statistics diverge for different  $\lambda_c$  rapidly. The variables of these simulations one turnover time after the injection can be found in table 1. In Fig. 8 the kinetic energy of the particles is displayed. As  $\lambda_c$  rises, the decay in the kinetic energy of the particles becomes smaller. This behavior leads to the assumption that the clustering produces the behavior of heavy particles as the results fit to the findings of Schneiders [?]. Fig. 9 can be used to point out the difference between the results for LES and DNS. It is evident that a correlation between inaccuracy of the simulations and the refinement level of the grid exists. For the same ratio of physical point particles to CPPs

$\lambda_c$	$\frac{m_c}{m_{V,\text{cell}}}$	$\epsilon \frac{u_0^3}{L}$	$\frac{\lambda}{L}$	$\frac{\eta}{L}$	$Re_\lambda$
1	16.78	0.97	0.039	0.0032	38.73
10	167.78	2.08	0.028	0.0026	28.66
50	838.86	3.51	0.024	0.0023	27.31
100	1677.72	3.51	0.025	0.0023	29.42

Table 1: Variables of the first set of simulations one turnover time after injection for the  $256^3$ -case

the results show different behavior depending on the grid refinement level. The unclustered PP-case is included as reference. With  $\lambda_c = 50$  being a relatively high ratio the  $LES_{64}$  shows the most similar results, the DNS shows a large difference. This is due to the number of cells the force of the particles is projected on, which grows for each refinement step. It is therefore less critical to cluster particles in lower-resolution grids, although the results are not nearly as accurate as for the unclustered simulations.

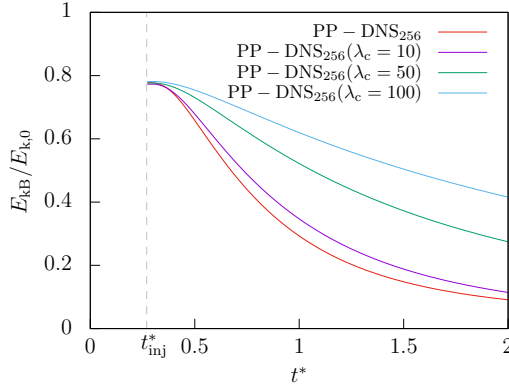


Figure 8: Kinetic energy of the particles  $E_{kB}$  normalized by initial kinetic energy. The PP-case without clustering shows the biggest decay in kinetic energy.

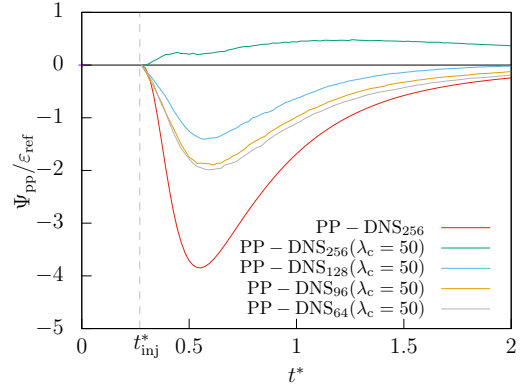


Figure 9: Point-particle coupling rate  $\Psi_{pp}$  with constant  $\lambda_c$  for various resolutions. A relation of resolution and accuracy can be observed.

The computational savings of this method may be present, their effect is not as prevalent as it needs to be to compensate the inaccurate results.

## 5 Conclusion and outlook

In this work, two sets of simulations were carried out to evaluate a method for lowering computational effort.

The results presented in this work show that for a sufficiently exact simulation particle clustering has to be treated with caution. Depending on the application maybe small numbers of clustered particles could be used, but the savings in computing time would not compensate the loss in accuracy. This is the case in particular high numbers of clustered particles at which the results get highly inaccurate. Maybe investigations on smaller numbers of clustered particles could follow, the space between 2 and 10 could be closed by simulations in the future to determine the real border for inaccurate results.

Further investigation is needed regarding the second set of simulation (Fig. 3), in which the goal was to find out which number of particles is necessary to get accurate results for the turbulent kinetic energy of the particles. The deviation of the averaged kinetic energy of the particles and the fluid should be zero. This difference converges to zero with high numbers of particles. The distribution of the experiment's outcomes should match the well-known normal distribution, which leads to analyzing the standard deviation. Concluding, further simulations should be carried out until a sufficient standard deviation can be computed, from which an assumption about the accuracy of the initialization could be made.

## 6 References

- [1] A. Ferrante and S. Elghobashi. On the physical mechanisms of two-way coupling in particle-laden isotropic turbulence. *Phys. Fluids*, 15(2):315–329, 2003.
- [2] A. Prosperetti and G. Tryggvason. *Computational methods for multiphase flow*. Cambridge University Press, 2009.
- [3] A.N. Kolmogorov. The local structure of turbulence in incompressible viscous fluid for very large Reynolds numbers. 30(4):299–303, 1941.
- [4] C. Siewert. *Numerical Analysis of Particle Collisions in Isotropic Turbulence*. PhD thesis, 2014.
- [5] D. Hartmann, M. Meinke and W. Schröder. An adaptive multilevel multi-grid formulation for Cartesian hierarchical grid methods. *Comput. Fluids*, 37(9):1103–1125, 2008.
- [6] D. Hartmann, M. Meinke and W. Schröder. A strictly conservative Cartesian cut-cell method for compressible viscous flows on adaptive grids. *Comput. Methods in Appl. Mech. Eng.*, 200(9):1038–1052, 2011.
- [7] Van Dyke. *An album of fluid motion*. Parabolic Press Stanford, 1982.
- [8] J.R. Fessler, J.D. Kulick and J.K. Eaton. Preferential concentration of heavy particles in a turbulent channel flow. *Phys. Fluids*, 6(11):3742–3749, 1994.
- [9] K. Fröhlich, L. Schneiders, M. Meinke and W. Schröder. Validation of Particle-Laden Large-Eddy Simulation Using HPC Systems. In *Sustained Simulation Performance 2017*, pages 137–149. Springer, 2017.
- [10] L. Schneiders, M. Meinke and W. Schröder. Direct particle–fluid simulation of kolmogorov-length-scale size particles in decaying isotropic turbulence. *J. Fluid Mech.*, 819:188–227, 2017.
- [11] L.F. Richardson. The supply of energy from and to atmospheric eddies. *Proceedings of the Royal Society of London. Series A, Containing Papers of a Mathematical and Physical Character*, 97(686):354–373, 1920.
- [12] M.R. Maxey and J.J. Riley. Equation of motion for a small rigid sphere in a nonuniform flow. *Phys. Fluids*, 26(4):883–889, 1983.

- [13] S. B. Pope. *Turbulent flows*. Cambridge University Press, 2000.
- [14] S. Elghobashi. Particle-laden turbulent flows: direct simulation and closure models. *Appl. Sci. Res.*, 48(3):301–314, 1991.
- [15] S. Elghobashi. On predicting particle-laden turbulent flows. *Appl. Sci. Res.*, 52(4):309–329, 1994.
- [16] S. Hickel. *Implicit turbulence modeling for large-eddy simulation*. PhD thesis, 2008.
- [17] V. Armenio and V. Fiorotto. The importance of the forces acting on particles in turbulent flows. *Phys. Fluids*, 13(8):2437–2440, 2001.

## 7 Appendix A

### Creating of pictures showing tubular structures

The pictures used in to point out the differences between DNS and LES were generated using ParaView, an open-source-software developed by a joint-venture of Kitware and the Los Alamos National Laboratory. More information about the software can be found at [www.paraview.org](http://www.paraview.org). To show the tubular structures in a turbulent flow, two filters were used: One was the AIALambda2Criterion1-Filter and the other one was the ISOVolume1-Filter. These filters were then set to visualize the velocity of the flow colored by magnitude. To diversify the different velocity-magnitudes, a rainbow-colorscheme was used.